Non-metastatic para-aortic lymph node remodeling as a predictor of outcome in locally advanced cervical cancer

Louis Baudin[1,*], Léa Zanella[1,*], Alizée Lebeau[2,3], Clémence Pleyers[4], Noémie Gubbels[1], Silvia Blacher[1], Laurence Seidel[5], Athanasios Kakkos[2], Frédéric Goffin[2], Pierre Lovinfosse[6], Christine Gennigens[3], Sébastien Pirson[1], Frédéric Kridelka[2, #] and Agnès Noel[1,#,δ]

[1] Laboratory of Tumor and Development Biology, GIGA, University of Liège (ULiège), Avenue Hippocrate 13, Sart-Tilman, B-4000, Liège, Belgium.

[2] Department of Obstetrics and Gynecology, University Hospital of Liege (CHU-Liège), Sart-Tilman, B-4000, Liège, Belgium.

[3] Department of Medical Oncology, University Hospital of Liège (CHU-Liège), Sart-Tilman, B-4000, Liège, Belgium.

[4] Department of Oncological Radiotherapy, University Hospital of Namur (CHU-UCL-Namur), B-5530, Namur, Belgium

[5] Biostatistics and Research Method Center (B-STAT), CHU-ULiège, Avenue Hippocrate 13, Sart-Tilman, B-4000, Liège, Belgium.

[6] Department of Nuclear Medicine and Oncological Imaging, University Hospital of Liège (CHU-Liège), Sart-Tilman, B- 4000, Liège, Belgium.

* Contributed equally to the work; # Co-senior authors

[δ] **Corresponding author:** Agnès Noel, Laboratory of Tumor and Development Biology, Tour de Pathologie, B23, +4; Avenue Hippocrate, 13, 4000 Liège, Belgium.
Email: agnes.noel@uliege.be

Running title: predictive value of para-aortic lymph node in LACC

ABSTRACT

Purpose: Treatment of Locally Advanced Cervical Cancer (LACC) is guided notably by the European Society of Gynaecological Oncology (ESGO) guidelines; unfortunately, relapse remains frequent despite standard chemoradiotherapy and brachytherapy. We evaluated whether histological assessment of non-metastatic para-aortic lymph node (PAoLN) provides prognostic value in LACC.

Experimental design: Primary tumor and PAoLNs from 137 non-metastatic LACC patients were stratified by pre-therapeutic 18F-FDG PET/CT into pelvic PET-positive (pPET+, N= 72) and negative (pPET-, N= 65) groups. Immunohistochemistry on whole sections assessed germinal centers, CD4+, CD8+, FOXP3+ cells, neutrophils (CD66b+, neutrophil extracellular traps: NETs) and high-endothelial venules (HEVs). Associations with progression-free survival (PFS) were examined via univariate and multivariate analyses after a median follow-up of 55.4 months.

Results: Primary tumor profile was not associated with outcome, whereas PAoLN features were strongly predictive. In pPET- patients, higher NETs were associated with shorter PFS (p=0.015; HR=2.768), while elevated CD4/CD8 ratio improved outcomes (p=0.047, HR=0.497). In pPET+ patients, shorter PFS was linked to FOXP3+ (p=0.04, HR=1.918) and proliferating FOXP3+ cells (p=0.018, HR=1.668) density. Across the full cohort, abundant germinal centers (p=0.0355, HR=0.273) and elevated CD4/CD8 ratio (p=0.001, HR=0.490) independently correlated with lower recurrence risk. Internal validation was conducted through a bootstrap resampling method. Combinatorial analyses revealed distinct predictive signatures according to pPET status: higher NETs, fewer germinal centers and FIGO-IIA1-IIIB status predicted relapse in pPET- patients.

Conclusions: Integrating pPET status with PAoLN histological analyses improves recurrence risk stratification in LACC. PAoLN evaluation may serve as a complementary tool to guide treatment intensification and surveillance strategies.

TRANSLATIONAL RELEVANCE

Despite multimodal therapy, patients with Locally Advanced Cervical Cancer (LACC) face a high risk of relapse, and current International Federation of Gynaecology and Obstetrics (FIGO) 2018 staging provides limited prognostic discrimination. Our study demonstrates that histologic evaluation of para-aortic lymph nodes (PAoLNs), when integrated with pelvic 18F-FDG PET/CT status, refines recurrence risk assessment beyond conventional staging. Distinct immune signatures in PAoLNs—particularly germinal center activity, FOXP3+ T-cell expansion, CD4/CD8 ratio and neutrophil extracellular trap (NET) density—identified subgroups of patients with differential relapse risk. The global multivariate model was translated into a nomogram incorporating three factors to facilitate individualized risk assessment in clinical practice. These findings highlight the clinical value of PAoLN immune profiling as a complementary biomarker strategy, which may enable more precise stratification of patients for treatment intensification or tailored surveillance.

INTRODUCTION

Cervical cancer accounts for approximately 660,000 new cases and 350,000 deaths annually, ranking as the fourth most common malignancy and cause of cancer-related mortality among women worldwide (1). Notably, it is the second leading cause of cancer death among women aged 18 to 44 years across both high-income and low- to middle-income countries (GLOBOCAN 2022). The clinical management and prognosis of cervical cancer are guided by the disease stage as defined by the International Federation of Gynaecology and Obstetrics (FIGO) classification system (2). The disease progresses from early-stage, defined by tumors <4cm confined to the cervix, to locally advanced cervical carcinoma (LACC), characterized by tumors >4cm and/or extension into adjacent pelvic structures. In 2018, the FIGO staging system was revised to incorporate imaging and pathological findings, including the lymph node (LN) status (not metastatic [M0]/metastatic [M+]) due to their prognostic significance. The detection of LN metastases by imaging modalities automatically upstages the FIGO stage IIIC1 for pelvic LN to stage IIIC2 for para-aortic LNs (PAoLNs), irrespective of primary tumor size or local spread. Indeed, LN involvement is a strong prognostic factor, associated with higher recurrence risk and poorer overall survival (3–6). According to European Society of Gynaecological Oncology (ESGO)/European Society for Radiotherapy and Oncology (ESTRO)/European Society of Pathology (ESP) guidelines, the standard treatment for LACC (FIGO 2018 stage IB3 to IVA) consists of cisplatin-based concurrent chemoradiotherapy followed by brachytherapy. Treatment is further tailored according to the nodal status assessed either by pre-therapeutic positron emission tomography/computed tomography using ^{18}F-2′-deoxy-2′ fluorodeoxyglucose (^{18}F-FDG PET/CT) imaging (referred below as PET) or by LN surgical staging. In cases of nodal involvement, management may include an external beam radiotherapy boost (EBR) to the affected LN, and extended-field of radiotherapy to the para-aortic (PAo) area

(7). In the current era of treatment de-escalation and precision surgery, the role of PAo

lymphadenectomy is increasingly being questioned, particularly in patients with negative PET findings. Indeed, this surgical procedure is associated with increased complications and morbidity, and its diagnostic and therapeutic benefit remains unclear (8–11). Despite advances in multimodal treatment, including surgical staging, about one-third of LACC patients treated with concurrent chemoradiotherapy and brachytherapy experience recurrence (12,13).

The persistent risk of relapse highlights the need to identify reliable risk-signatures at diagnosis, ideally within primary tumors and/or within PAoLNs, to improve recurrence risk stratification in patients with LACC and individualize their treatment. In this study, we investigated immunological modulation within the primary tumor and PAoLN at the time of diagnosis, focusing on key immune variables including B-cell germinal centers, CD4+, CD8+, and FOXP3+ T cells, neutrophils, neutrophil extracellular traps (NETs), and high-endothelial venules (HEVs) as a critical regulator of lymphocyte trafficking and immune surveillance. We evaluated whether immunological alterations varied within PAoLN of patients with positive *vs* negative pelvic PET (pPET) findings and correlated with clinical outcomes. Primary tumors were also analyzed to assess corresponding histopathological features. We provide evidence that pelvic PET scan status, when integrated with PAoLN analyses, but not primary tumor features, is a reliable predictor of recurrence risk. Our study highlights the added value of PAoLN staging to identify LACC patients most likely to benefit from treatment intensification and/or more cautious follow-up.

MATERIEL AND METHODS

Human tissue samples

The retrospective single-center cohort included 155 female patients diagnosed with LACC and treated at the University Hospital of Liège (Belgium) between May 2010 and April 2022. Median age was 52 years. LACC stage was defined according to FIGO 2018 classification (IB3 to IVA). To be eligible, patients must (i) have received a diagnostic/pre-treatment PET scan (ii) have undergone laparoscopic para-aortic lymphadenectomy, (iii) have been treated with concomitant chemoradiotherapy (CCRT) followed by brachytherapy, and (iv) have no detectable metastasis in PAoLNs through histological examination. The overall prevalence of HPV-positivity was 98%. Given this minimal variability in HPV status, particularly within the SCC subgroup, in which all tumors were HPV+, HPV infection was not included as an independent covariate in the multivariable models, as its near-uniform distribution precluded meaningful stratified or adjusted analyses (**Supplementary Table S1**).

Formalin-fixed, paraffin-embedded (FFPE) LNs and/or primary tumor samples collected before treatment were available for all patients and provided by the Biobank of the University Hospital of Liège (Belgium). All specimens were reviewed by experienced pathologists and classified as metastatic or non-metastatic. Clinical and pathological data were retrieved from electronic medical records. Patients with incomplete clinical data or unavailable tissue material were excluded.

The study protocol was approved by the Institutional Ethics Committee of the University Hospital of Liège (2024-438). The use of human body material from the biobank does not require consent forms (Belgian law of 19 December 2008).

Immunofluorescence on human LN sections

PAoLN and primary tumor biopsies from patients with LACC were fixed in formaldehyde 4% directly after lymphadenectomy or tumor biopsy, respectively. Then, they were paraffin-

embedded and sectioned at 4µm. Tissue sections were rehydrated through successive xylene, alcohol and water baths. Heat-induced antigen retrieval was performed using Dako target retrieval buffer at pH 9.0 (Dako, S2367). After cooling for 20 min and rinsing with water, non-specific background noise was reduced using TrueBlack (Cell Signaling, 92401 S). Slides were then blocked with animal-free blocking solution (Cell Signaling, 15019 L) for 30min, followed by incubation with the primary antibody of interest diluted in antibody diluent (Dako, S2022) for 1h at room temperature or overnight at 4°C, in a humidified darkroom. Samples were washed with PBS and incubated with the appropriate secondary antibody. These steps were repeated for combined stainings. Slides were mounted with DAPI mounting media (SouthernBiotech, 0100-20).

Different combinations of antibodies were applied on serial sections of primary tumors and PAoLNs. Primary tumor sections were labeled with combinations of CD4/CD8/αSMA/cytokeratin, CD66b/FOXP3/cytokeratin/αSMA, and PNAd/cytokeratin/αSMA. For PAoLNs, stainings included PNAd, CD4/CD8, CD66b/FOXP3/Ki67, and H3cit/MPO.

The antibodies and all associated informations are listed in **Supplementary Table S2**.

Virtual image acquisition and quantification

Virtual images were acquired with SLIDEVIEW VS200 from Olympus at 20x magnification (Olympus, Anvers, Belgium) equipped with a UPlan-XApo 20× 0.8× objective (Olympus) and with a Hamamatsu ORCA-Flash camera, using DAPI, FITC, Cy3, Cy5 and Cy7 filter sets. All quantitative analyses were conducted on whole tissue sections using QuPath software v0.5.1 (RRID: SCR_018257) to determine either the stained area or the number of positive cells/structures (HEV, germinal center). For CD4 and CD8 positive cell evaluation, density was defined as the ratio of the stained area to the stromal section area. For FOXP3+ cells, CD66b+ cells, NETs, germinal centers and HEVs, density represents cell/structure number/mm^2.

Regarding primary tumor samples, stromal *vs* tumor segmentation was computationally

performed based on cytokeratin positivity. Tumor-Associated High Endothelial Venules (TA-HEVs) were defined as an object displaying a lumen and covered by αSMA+ cells and PNAd detection in the lumen side.

For PAoLN samples, the total number of HEVs was automatically counted by detecting every PNAd+ structures larger than 100µm² to omit putative artefactual objects. Lumenized HEVs were hand-detected and their lumen were measured manually. To decrease the slice sectioning bias, the smallest diameter was considered for complex vessels. Dilated HEVs are defined as HEVs displaying a lumen over 20µm. 36841 HEVs and 2475 dilated HEVs were analyzed for pPET- and 52748 HEVs and 2204 dilated HEVs for pPET+ patient groups. Results were expressed as percentage of dilated HEVs. NETs were quantified based on the colocalization of myeloperoxidase and citrullinated histone H3 staining.

Statistical methods

All the data were tested for normality by the Shapiro-Wilk test. Some parameters were log-transformed (LN) or square-root transformed (SQ) before their use in statistical models. Comparisons between groups were done with the Kruskal-Wallis H test followed by Dunn's multiple comparison or the Mann-Whitney U test as specified in the figure legends. Data are shown using the median with interquartile ranges. Statistical significance was determined at $p<0.05$, denoted as follows: *$p<0.05$, **$p<0.01$, ***$p<0.001$, ****$p<0.0001$.

The association between continuous variables was assessed using Spearman's Rank correlation coefficient (r_s). To identify the most predictive signatures of relapse derived from multiple parameters, we applied an unbiased, combinatorial Cox regression-based predictive model approach. First, each parameter was evaluated individually (univariate analysis). Next, all possible pairwise (2X2) and triplet (3X3) combinations were assessed. To prevent the generation of subgroups too small for meaningful statistical interpretation, we applied a minimum threshold of 6 patients per group (approximately 10% of both the pPET- and pPET+ population). For each tested combination, two subgroups were generated: (i) patients meeting

all combined criteria, and (ii) all remaining patients. For every subgroup, we recorded the total number of patients, the number of relapse events and the corresponding p-value. Table A (**Supplementary Figures S1, S2**) reports the data for each variable analyzed independently, while Tables B and C present only the data those parameter combinations that significantly predicted relapse of the respective subgroups. All the used cut-off values are indicated in the figures, which correspond to the median of each patient group (pPET- and pPET+) when considering continuous variables.

Progression-free survival (PFS) was analyzed according to the studied continuous variables (group-related) using Cox proportional hazards regression. The Schoenfeld residuals test was performed for each model to assess the proportional hazards (PH) assumption. In cases where the PH assumption was not met (in red in the tables), the model was corrected by adding an interaction term between the parameter and time (interval between staging and relapse/last follow-up). Variables with a p-value <0.10 in univariate analysis were then included in the multivariate model. When the PH assumption was not met in univariate analysis, both the variable and the variable × time interaction were entered into the model if the variable remained significant after correction. Multivariate Cox regression with stepwise selection was subsequently applied to the selected variables. In some instances, Firth's correction was used. For univariate and multivariate analyses, the p-value, the hazard ratio (HR) with its 95% confidence interval (CI), the results of the PH test, and the adjusted p-values were reported for each variable. Multivariate analyses display only the statistically significant variables ($p<0.05$). Statistical significance was set at a two-sided 5% level ($p<0.05$). The dataset was bootstrapped 500 times to check the stability of the multivariate models. The model was applied on each resampling and the Harrel's C-index was derived. The mean and standard deviation of the 500 obtained C-indexes were calculated to give an estimation of the mean and the precision (standard error) of the original model. Multivariate Cox proportional hazards models were constructed by integrating clinical parameters, PET imaging status, and PAoLN

immune/vascular features identified as significant in univariate analyses. Area under the curve (AUC) over time was graphically reported to assess prognostic performance throughout follow-up. Nomogram was generated from the final multivariable models to provide individualized estimates of progression-free survival at 12, 24, and 36 months. Cumulative incidence functions (CIFs) were estimated within a competing risks framework. Local-regional (LRR) and distant recurrences (DR) were considered as distinct failure types, while patients without recurrence were treated as censored. CIFs were computed using the Fine and Gray subdistribution hazard approach, providing direct estimates of the probability of each recurrence type over time. These time-dependent incidence estimates were subsequently combined with recurrence site information to construct time-resolved failure maps, allowing spatial visualization of recurrence patterns across follow-up.

Statistical analyses were performed using GraphPad Prism 9.0 (GraphPad Software, RRID: SCR_002798), SAS version 9.4 (RRID: SCR_008567) and R version 4.5.1 (RRID: SCR-001905).

Data availability statement

Material used to conduct the research and all data supporting the findings of this study are included in this article and its Supplementary Materials. Whole-slide immunohistochemical images are not publicly deposited due to their substantial file size and ethical restrictions associated with patient-derived material. Access to these data may be considered for academic research purposes upon reasonable request to the corresponding author and subject to institutional review and applicable data protection regulations. Quantitative image analyses were performed using the publicly available software QuPath. No custom code or proprietary algorithms were generated for this study. Deidentified clinical summary data may be shared for academic, non-commercial research purposes, upon request to the corresponding author, and in accordance with institutional review board approval and relevant data protection legislation.

RESULTS

Workflow of the study

In cervical cancer, most metastases typically progress stepwise, spreading from the pelvic region (primary tumor and pelvic LNs) to the PAoLNs. Patient cohort and sample overview are schematically illustrated in **Figure 1**, with PAoLN metastasis assessed histologically (PAoLN+ *vs* PAoLN-) (**Figure 1A**) and PET scan used to classify patients as negative (pPET-) or positive (pPET+) pelvic nodes (**Figure 1B**). Primary tumor and PAoLN samples were subsequently analyzed via immunohistochemistry (IHC) (**Figure 1C**) for key immune and stromal markers to identify microenvironmental signatures associated with recurrence risk. To ensure an unbiased approach and consider tissue heterogeneity, stained samples were whole-scanned and subjected to semi-automatic computerized quantification (**Figure 1C**).

Between 2010 and 2022, 155 patients with LACC were treated at the University Hospital of Liège (**Figure 1D**). Eighteen patients with para-aortic metastases at diagnosis were excluded, resulting in 137 eligible patients. The cohort was divided into two subgroups: 72 patients classified as pPET– (no pelvic node uptake) and 65 as pPET+ (pelvic node uptake). Biomarker analyses were performed in all 137 patients using pretreatment samples obtained at diagnosis. For survival analyses, 7 patients who received additional treatments were excluded to obtain a final cohort of 130 patients uniformly treated with CCRT followed by image-guided brachytherapy (IGBT).

The clinical and pathological characteristics of the patients are summarized in **Supplementary Table S3**. Median age was 52 years. All patients underwent para-aortic staging allowing to confirm para-aortic negative status (PAoLN-). Squamous cell carcinoma (SCC) was the predominant histological subtype (84.7%). FIGO stages IIIC1 to IVA represented 50% of cases, followed by IIA1-IIIB (35.8%) and IB3 (13.1%). Median tumor size on MRI was 48 mm (interquartile range: 39–56 mm). The median interval time from staging to treatment completion was 2.4 months. On PET scan, pelvic LNs were considered positive

and negative in 52.5% and 47.4%, respectively. pPET scan positivity in patients treated with combined CCRT and IGBT conferred a two-fold higher risk of recurrence (HR [95% CI]: 2.251 [1.139-4.451]) (**Figure 1E**), underscoring its association with adverse prognosis in LACC patients. Given that pPET scan status was predictive of recurrence and patient characteristics were well-balanced (**Supplementary Table S3)**, all analyses were stratified according to pPET+ and pPET– groups.

The median follow-up was 55.4 months. The five-year overall survival (OS) and progression-free survival (PFS) were 73.83% and 72.53%, respectively. During follow-up, recurrence was observed in 34 patients (26.2%), and 28 patients (21.5%) died from cancer.

T cell infiltration profile differs in primary tumors of patients according to pPET status. IHC were conducted on the available primary tumor samples obtained from patients with non-metastatic PAoLN disease (PAoLN-) (N=91). Immune markers were quantified within the stromal compartment delineated through cytokeratin staining (**Figure 2A-C**). The CD4/CD8 ratio was significantly reduced in patients with positive pPET scan (**Figure 2D**). This may be explained by CD8 density that tended to increase in these patients, while CD4 density was similar in pPET+ and pPET- patients (**Figure 2E, F**). Densities of FOXP3+ cell and CD66b+ cells were indistinguishable between the two patient groups (**Figure 2G, H**). These results reflect a differential profile of CD8-T cell infiltration in the tumor stroma of patients according to pPET status.

The pattern of tumor-associated HEVs differs according to pPET status.

Given their established role in immune cell recruitment, we also quantified the density of Tumor-Associated HEVs (TA-HEVs), defined as lumenized peripheral node addressin positive vascular structures (PNAd+ vessels) covered by alpha smooth muscle actin-positive (αSMA+) cells, within the tumor stroma (**Figure 2I**). Based on the median and quartile distribution of TA-HEV density, samples were classified into four categories: class I (0 vessels/mm²), class II (0-1.173 vessels/mm²), class III (1.173-4.362 vessels/mm²) and class IV (4.362-22.644

vessels/mm²) (**Figure 2J**). Overall, PNAd+ vessel density tended to decrease in pPET+ group compared to pPET-, although this difference did not reach statistical significance (**Figure 2K**). When stratifying by TA-HEV class, tumors from pPET+ patients display a shift toward lower TA-HEV classes, with an enrichment in classes I and II (58%) and a relative reduction in classes III and IV (32%) (**Figure 2L**). In contrast, tumors of pPET- patients showed the opposite distribution (43.5% of classes I + II and 56.5% of classes III + IV).

We next examined the relationship between TA-HEV classes and immune cell infiltration (**Figure 2M-P**). In pPET- patients, higher TA-HEV classes were associated with increased densities of both CD8 and CD4 ($p<0.05$) (**Figure 2M, N**). In contrast, in pPET+ patients, T cell densities remained stable across all vessel classes. CD66b+ or FOXP3+ cell infiltration did not vary significantly across TA-HEV classes or between patient groups (**Figure 2O, P**). Nonetheless, TA-HEV density showed a weak but significant positive correlation with CD4+ cell density (Spearman's $r_s= 0.2467$, $p= 0.0191$), whereas no such correlation was found with CD66b, FOXP3, or CD8 cell densities. Collectively, these findings indicate that TA-HEVs exhibit distinct patterns in the tumor stroma of pPET+ *vs* pPET- patients, but their relationship with immune cell infiltration remains limited.

Primary tumor profiles are not associated with relapse risk in univariate analyses

PFS was evaluated using Cox regression for each parameter assessed on the primary tumor. All biological variables and clinical characteristics were included in the analysis (**Supplementary Table S4**). Univariate analyses of the primary tumor did not identify any variables as prognostic indicators of relapse when patients were stratified according to pPET status (**Supplementary Table S4**). Univariate followed by multivariate analyses were performed on all available primary tumor samples uniformly treated with CCRT + IGBT (N=87). The multivariate analysis revealed that tumor size was negatively correlated with PFS (p=0.0147; HR [95% CI]: 1.071 [1.014-1.132]), while elevated FOXP3+ cell density was protective (p=0.0267; HR [95% CI]: 0.623 [0.410-0.947]). Therefore, we decided to apply a similar methodology to PAoLNs- to

assess their impact. The clinical and pathological characteristics of the patients for these analyses are summarized in **Supplementary Table S5**.

PAoLNs of pPET+ patients display a more dynamic immune response

We next focused our study on non-metastatic PAoLNs of pPET+ and pPET- LACC patients (n=129) (Supplementary Figure S1). The number of germinal centers was higher in pPET+ patients compared to pPET- patients, suggesting a more dynamic immune response in the former group (Figure 3A). The density of CD4+ cells was comparable between the two patient groups. However, the CD4/CD8 ratio tended to be lower in PET+ samples, likely driven by a modest, though not statistically significant, increase in CD8+ cell density ($p>0.05$, Figure 3B-D). In contrast, FOXP3+ cells and proliferating FOXP3+Ki67+ cells were significantly enriched in pPET+ patients ($p<0.01$ and $p<0.05$, respectively) (Figure 3E, F). To accurately assess neutrophil involvement (infiltration and activity), we immunostained CD66b+ cells and detected NETs through both citrullinated histone 3 (H3Cit) and myeloperoxidase (MPO) stainings, on serial sections (Figure 3G-H). CD66b+ cell density was significantly enhanced in pPET+ patients ($p<0.05$), accompanied by a trend towards increased NET formation (Figure 3G, H).

Finally, we evaluated HEVs, specialized vascular structures within LNs that facilitate lymphocyte trafficking. Under inflammatory or tumoral conditions, HEVs can become dilated (lumen > 20μm), a change thought to impair immune cell recruitment (14). The proportion of dilated HEVs did not differ significantly between the two patient groups ($p=0.055$) **(Figure 3I)**. Notably, the frequency of dilated HEV correlated negatively with CD8+ cell density (Spearman's $r_s= 0.2319$, $p= 0.0098$), but showed no significant association with CD4+, CD66b+ cell or FOXP3+ cell densities ($p>0.05$, **Figure 3J-M**). In conclusion, non-metastatic PAoLNs of pPET+ patients display features of increased immune activity—including increased germinal center formation, FOXP3+ cell expansion, neutrophil infiltration—while preserving HEV architecture that likely supports sustained lymphocyte recruitment.

Multivariate and univariate analyses in the PAoLN

PFS was evaluated in relation to clinical parameters (pPET, histology, FIGO stage, age, tumor size) and PAoLN biological features (neutrophils, NETs, FOXP3+ cells, FOXP3+Ki67+ cells, germinal centers, CD4/CD8 ratio, dilated HEVs). The corresponding clinical and pathological characteristics of patients are summarized in **Supplementary Table S5**. For pPET- patients, univariate analyses identified NETs (p=0.015; HR [95% CI]: 2.768 [1.215-6.304]) and CD4/CD8 ratio (p=0.047; HR [95% CI]: 0.497 [0.250-0.989]) as prognostic markers (**Table 1**). In contrast, the relapse risk of pPET+ patients were found to be significantly associated with FOXP3+ (p=0.04; HR [95% CI]: 1.918 [1.029-3.575]), FOXP3+Ki67+ (proliferating FOXP3+ cells) (p=0.018; HR [95% CI]: 1.668 [1.093-2.544]) cell densities, as well as CD4/CD8 ratio (p=0.0097; HR [95% CI]: 0.506 [0.302-0.848]) (**Table 1**).

We then performed a multivariate analysis on the available samples from the global cohort independently of pPET status (N=123), selecting variables with p<0.1 from the univariate analyses (**Table 1**). pPET positivity emerged as an independent predictive factor, (p=0.0033; HR [95% CI]: 3.299 [1.488-7.315]), being significantly associated with an increased risk of relapse. Conversely, a high number of germinal centers (p=0.0355; HR [95% CI]: 0.273 [0.081-0.915]) and a high CD4/CD8 ratio (p=0.001; HR [95% CI]: 0.490 [0.320-0.748]) were independently associated with a better PFS. For pPET+ subgroup, we explored the use of continuous PET parameters including Standardized Uptake Value maximum (SUVmax), Metabolic Tumor Volume (MTV), Total Lesion Glycolysis (TLG). This approach did not improve model performance compared to the binary pPET+ *vs* pPET– classification (**Supplementary Figure S6**). Internal validation of our model was performed using the bootstrap resampling method with 500 iterations to assess model stability and correct for optimism. The apparent model performance yielded a Harrel's C-index of 0.7434. After bootstrap validation, the optimism-corrected mean (SE) C-index was 0.7536 (0.045), indicating a stable

discriminating performance with minimal overfitting.

Integrated predictive model and clinical applicability

Time-dependent AUC analysis (**Figure 4A**) showed that the model displayed a good and stable discriminative ability over time. After an initial period of instability during the early follow-up, likely related to a limited number of events, the AUC rapidly increased and remained consistently around 0.75–0.80 throughout follow-up, indicating a robust capacity to discriminate patients according to their risk of recurrence. To integrate clinical, imaging, and PAoLN immune features into a unified prognostic framework, we performed multivariable regression analyses incorporating pPET status, the number of germinal centers, and the CD4/CD8 ratio, which were independently associated with progression-free survival. Based on the final multivariable model, we constructed a nomogram for the global cohort (N = 123) to enable individualized prediction of PFS probabilities at 12, 24, and 36 months (**Figure 4B**).

Distant recurrence is the predominant type of early therapeutic failure

Recurrences occurring after treatment were categorized as locoregional (LRR; in local tissues and pelvic LNs) or distant (DR; in PAoLNs and extra-nodal organs outside the pelvis). Across the whole cohort, DR represents the predominant mode of therapeutic failure over time, with a CIF of 0.10 at 12 months, compared with LRR, which shows a CIF of 0.05 (**Figure 4C**). Accordingly, one year after initial staging and treatment, 10% of patients experienced a distant relapse, 5% relapsed in the pelvic region, while 85% remained recurrence-free. The predominance of DR over LRR was confirmed after dichotomization according to pPET status. Among pPET+ patients, at 12 months, 15% and 10% of patients experienced DR and LRR, respectively. In contrast, among pPET- patients, despite an overall reduction in the total number of recurrences, the 12-month CIF was 8% for DR and 0% for LRR. Collectively, these time-to-failure patterns suggest that DR occurs more

frequently and earlier than LRR, which may reflect effective local disease control and/or more aggressive phenotypes favorable to systemic dissemination.

Distinct prognostic profiles predict relapse risk in pPET- and pPET+ patients.

We conducted a combinatorial Cox regression-based analysis to assess the existence of high-risk patient subgroups within both pPET- and pPET+ groups. Following median-based univariate analyses, successive evaluations were performed to generate all possible combinations of two or three variables (**Supplementary Tables S7, S8**). In pPET+ patients, univariate analysis revealed that a low CD4/CD8 ratio (p=0.0092; HR [95% CI]: 3.811 [1.392-10.434]) or high FOXP3+Ki67+ cell density (p=0.0369; HR [95% CI]: 2.743 [1.063-7.075]) were significantly associated with increased relapse risk (**Supplementary Table S7A**). When combining two variables, ten significant associations emerged, with the most relevant being CD4/CD8 ratio & germinal centers (p=0.0017; HR [95% CI]: 4.038 [1.691-9.640]), CD4/CD8 ratio & tumor size (p=0.0056; HR [95% CI]: 3.402 [1.1431-8.088]), CD4/CD8 ratio & FOXP3+ cell density (p=0.006; HR [95% CI]: 3.394 [1.420-8.113]) (**Supplementary Table S7B**). Strikingly, the addition of a third variable (CD4/CD8 ratio & FOXP3+ cells & germinal centers) identified a subgroup of patients with uniformly poorer outcomes, as all patients relapsed (p=0.0001; HR [95% CI]: 6.63 [2.613-16.817]) (**Figure 5A, Supplementary Table S7C**). Kaplan-Meier plot combining these three parameters clearly demonstrates a strong association between a low CD4/CD8 ratio, a reduced number of germinal centers and high FOXP3+ cell density with poor patient outcomes (**Figure 5B**).

In the pPET- group, univariate analysis identified NETs (p=0.0282; HR [95% CI]: 5.576 [1.202-25.875]) and the number of germinal centers (p=0.0472; HR [95% CI]: 4.721 [1.020-21.861]) as significantly associated with relapse risk (**Supplementary Table S8A**). Combination analyses revealed that NETs & germinal centers (p=0.0009; HR [95% CI]: 9.537 [2.510-36.235]), as well as NETs & FIGO IIA1-IIIB (p=0.0052; HR [95% CI]: 8.943 [1.923-41.591]) were the most relevant (**Supplementary Table S8B**). The most predictive model was

the combination of NETs & germinal centers & FIGO IIA1-IIIB, which conferred the highest

relapse risk (p=0.0003; HR [95% CI]: 12.068 [3.159-46.108]) (**Supplementary Table S8C**). The most relevant single, dual, and triple variable associations for pPET- patients are illustrated in **Figure 5D**. Kaplan-Meier plot combining three potent parameters demonstrates a strong association between a high NET density, a reduced number of germinal centers and FIGO IIA1-IIIB status with poor patient outcomes (**Figure 5E**).

The specificity, sensitivity and accuracy of each signature are presented in **Figure 5C, F** and **Supplementary Figures S7 and S8**. The signature related to pPET+ patients demonstrated a perfect positive predictive value (PPV=1.0) and specificity (1.0), reflecting an excellent capacity to correctly identify patients who relapsed without any false positives. Its sensitivity (0.38) and the negative predictive value (NPV) were moderate (0.73), indicating some cases of relapse were not detected (**Figure 5C**). The second signature for pPET- patients was more sensitive (0.73) with a lower PPV value (0.53) (**Figure 5F**).

Together, our combinatorial analyses revealed distinct predictive signatures in pPET- and pPET+ patients with LACC.

DISCUSSION

Despite significant progresses in the management of LACC over the past two decades, approximately 30% of patients still experience disease recurrence (15). Among known prognostic factors, nodal status plays a central role in treatment planning. In particular, the detection of PAoLN involvement remains critical, as it can lead to disease upstaging and prompt a change in the therapeutic strategy, which can include the use of extended-field radiotherapy (7). We hypothesized that, even in the absence of detectable metastatic cells and/or in the case of PET scan negativity at the PAo level, PAoLNs may contain valuable predictive information. A key originality of the present study lies in the in-depth histological and IHC analysis of whole-scanned sections of PAoLNs, which are typically disregarded once classified as metastasis-free. Our study demonstrates the added value of integrating pPET scan status and PAoLN histological analyses at diagnosis to predict the risk of relapse.

We conducted a retrospective cohort study of LACC patients, focusing on those with histopathologically negative PAoLN (N=137). Previous studies have demonstrated an increased risk of PAoLN disease when PET identifies positive pelvic nodes (16,17). Consistently, in our cohort, pelvic LN positivity assessed by imaging was associated with a two-fold increase in the risk of relapse. Based on this finding, we conducted a comparative analysis of PAoLN samples from patients with pPET positivity *versus* pPET negativity. We provide evidence that PAoLNs of patients with pPET positivity displayed enrichment in germinal centers, increased densities of total and proliferating FOXP3+ cells, and a reduced CD4/CD8 ratio. These data suggest a more dynamic and actively regulated immune microenvironment. In parallel, neutrophil density was elevated in these samples of pPET+ patients as demonstrated by CD66b+ immunodetection. This finding indicates increased innate immune cell infiltration, a phenomenon that remains poorly characterized both in LNs and in LACC (18). Evidence of NET formation, a hallmark of neutrophil activity, showed a positive trend, although it did not

reach statistical significance. This apparent discrepancy between neutrophil density and activity might be attributed to technical limitations, as reliable detection of NETs in LN tissue sections remains particularly challenging. To further explore LN remodeling, we investigated HEVs' architecture, specialized vascular structures in secondary lymphoid organs, composed of PNAd-expressing cuboidal endothelial cells (19,20). PNAd acts as a ligand for L-selectin/CD62L on lymphocytes, thereby mediating their adhesion to HEVs and subsequent entry into the LN. HEV dilation is a recognized alteration of LN architecture, occurring in both inflammatory and tumoral contexts (21). Bekkhus et al. reported HEV dilation in tumor-draining LNs of patients with invasive breast carcinoma (22). However, no major alterations of HEV architecture were observed in our cohort. Interestingly, CD8 density tended to increase in pPET+ patients and showed a negative correlation with HEV dilatation. This suggests that the preservation of structurally intact (less dilated) HEVs in these patients may support efficient CD8+ T cell recruitment into PAoLN, thereby sustaining local immune activity. In contrast, the enrichment of proliferating FOXP3+ cells in pPET+ patients was not linked to HEV dilation, suggesting that their local expansion is likely driven by in situ modulation rather than altered trafficking via HEVs. These findings support the notion that pPET positivity reflects not only tumor burden, but also an immunologically primed microenvironment in PAoLN, which may have implications in disease progression and therapeutic responsiveness.

Together our data reveal alterations in both adaptive (T cells) and innate (neutrophils) immune cell profiles within PAoLNs, even in the absence of detectable metastatic cells. These changes were accompanied by activation of the humoral immune response, evidenced by an increased number of germinal centers, sites where naive B lymphocytes differentiate into antibody-secreting memory B and plasma cells in response to T cell-dependent antigen. This observation is in line with our previous clinical study, which reported remodeling of B and T cell immune landscapes in non-metastatic pelvic sentinel LNs of patients with early-stage

cervical cancer (23). Collectively, these findings point to substantial modifications of LNs, occurring not only within the tumor-draining sentinel LN as predicted by the "pre-metastatic niche concept" (24), but also within more distant LNs (25).

In pPET+ patients, we identified a low CD4/CD8 ratio and a high FOXP3+Ki67+ cell density, either independently or in combination, as variables associated with an increased risk of relapse. Notably, the combined evaluation of CD4/CD8 ratio, FOXP3+ cell density, and number of germinal centers delineated a homogenous subgroup of patients with a 100% risk of disease progression (8/8 patients relapsed, 14% of pPET+ patients). Although the small sample size limits definitive conclusions, this pattern suggests that the immune features of the PAoLN microenvironment may critically impact clinical outcome. Importantly, the observed modulation of the LN immune microenvironment suggests a cascade-like immune response extending from the pelvic to the PAo regions. These data further support the interest of immunotherapy, particularly in pPET+ patients, which is increasingly considered for LACC treatment regardless of LN status (26–28). This is particularly relevant for cervical cancers, where persistent human papillomavirus (HPV) infection, detected in over 90% of cases, is a well-established driver of immune evasion (29). Our study supports the rationale for integrating immunotherapeutic strategies into the management of pPET+ patients, although the optimal immune checkpoint targets in this setting remain to be defined.

A key finding of the present study is the discovery of previously unrecognized variables, namely NETs and the number of germinal centers, that can independently, or in combination, predict a high-risk of relapse in pPET- patients. Notably, the combination of NETs, germinal center number and FIGO IIA1-IIIB stages demonstrated the strongest predictive value. These findings are highly relevant to clinical practice. Indeed, when PET scan on the pelvic area is negative, the clinical utility of PAoLN staging is currently debated, because the risk of PAo nodal involvement is very low as documented by Uzan et al. (16). Of note, previous studies have concluded that, in patients with negative pPET status, the risk of PAoLN metastasis is very

low (30,31). The clinical benefit of PAo lymphadenectomy is still debated and is currently being investigated in a phase III randomized clinical trial (PAROLA trial) (32). Although laparoscopic PAo lymphadenectomy is a well-codified technique, particularly in the hands of an experienced surgical team (33), it carries a risk of lymphatic and vascular morbidity and potential delay in treatment initiation that must be weighed carefully. Our novel findings suggest that PAoLN status after lymphadenectomy remains of interest in patients with negative pelvic LNs on imaging. Given the technical challenges for NET detection, germinal center quantification appears to be a more practical and reproducible approach for routine clinical use. We propose that closer surveillance would be beneficial for these patients. Since more than 75% of recurrences occur within the first 2–3 years after diagnosis, an intensified follow-up strategy during the high-risk window may be particularly valuable. Ultimately, follow-up schedules should be tailored to individual patients, taking into consideration prognostic factors, treatment modality and side effects. In this context, the development of a nomogram derived from the multivariate model represents a clinically meaningful step toward individualized risk stratification. Internal validation was provided using bootstrap resampling with 500 iterations. The temporal stability and robustness of the model are supported by time-dependent AUC values, achieving approximately 0.8 across follow-up. Collectively, these findings highlight the potential clinical utility of this approach to inform risk-adapted surveillance strategies in routine practice. A limitation of this LN study is its single-centered retrospective nature, analyzing only one LN among all resected by laparoscopy lymphadenectomy. Further validation on a prospective cohort would be necessary in future research.

Can we find similar information in the primary tumors and avoid PAo lymphadenectomy associated with post-operative complications (16)? In our cohort, a differential profile of CD8-T cell infiltration was noted in the tumor stroma of patients according to pPET status. Additionally, the density of TA-HEVs was distinguishable in tumors of pPET+ *vs* pPET- patients. However, TA-HEV density was not or very weakly correlated to immune infiltration.

Notably, none of the parameters analyzed or combinations tested were predictive of tumor relapse, except tumor size contributing to FIGO classification, and FOXP3+ cell density whose prognostic value appears controversial (34–37). These findings limit the possibility of using primary tumor features as reliable for relapse prediction and further support the clinical relevance of examining a combination of practicable and reproducible parameters in PAoLNs.

Together our study demonstrates the interest of combining clinical and histological variables to guide therapeutic decision-making, which is in line with the growing trend toward personalized medicine. These observations suggest that treatment strategies may need to be reconsidered or that closer surveillance should be implemented for patients identified as high risk.

AUTHORS' DISCLOSURES

The authors declare no conflicts of interest.

ACKNOWLEDGMENTS

The authors thank the Biobank of the University Hospital of Liège (Belgium) for providing human biopsies and Animascience for elaboration of the graphics. This work was supported by grants from the Fonds de la Recherche Scientifique - FNRS (F.R.S.-FNRS, Belgium), the Fondation contre le Cancer (foundation of public interest, Belgium), the Fonds spéciaux de la Recherche (University of Liège), the Fondation Hospitalo Universitaire Léon Fredericq (FHULF, University of Liège). This project has received funding from the FWO and F.R.S.-FNRS under the Excellence of Science programme (EOS No. 40007532). We thank the GIGA (Groupe Interdisciplinaire de Génoprotéomique Appliquée, University of Liege, Belgium) for the access to the various platforms: (1) GIGA-Genomics platform (2) GIGA-Proteomics platform (3) GIGA-Imaging and Flow Cytometry platform, (4) GIGA-Bioinformatics platform, and (5) GIGA-Mouse facility and Transgenics platform.

REFERENCES

1. Bray F, Laversanne M, Sung H, Ferlay J, Siegel RL, Soerjomataram I, et al. Global cancer statistics 2022: GLOBOCAN estimates of incidence and mortality worldwide for 36 cancers in 185 countries. CA: A Cancer Journal for Clinicians. 2024;74(3):229–63.

2. Bhatla N, Aoki D, Sharma DN, Sankaranarayanan R. Cancer of the cervix uteri. International Journal of Gynecology & Obstetrics. 2018;143(S2):22–36.

3. Wang W, Liu X, Meng Q, Zhang F, Hu K. Nomograms predicting survival and patterns of failure in patients with cervical cancer treated with concurrent chemoradiotherapy: A special focus on lymph nodes metastases. PLOS ONE. 2019 Apr 15;14(4):e0214498.

4. Guo T, Zhao Y, Zeng J, Li J, Tang E, Wu L. Examined lymph node counts affected the staging and survival in cervical cancer: a retrospective study using the SEER and Chinese cohort. Annals of Medicine. 2025 Dec 31;57(1):2459821.

5. Guani B, Mahiou K, Crestani A, Cibula D, Buda A, Gaillard T, et al. Clinical impact of low-volume lymph node metastases in early-stage cervical cancer: A comprehensive meta-analysis. Gynecologic Oncology. 2022 Feb;164(2):446–54.

6. Li J, Liu G, Luo J, Yan S, Ye P, Wang J, et al. Cervical cancer prognosis and related risk factors for patients with cervical cancer: a long-term retrospective cohort study. Sci Rep. 2022 Aug 17;12:13994.

7. Cibula D, Raspollini MR, Planchamp F, Centeno C, Chargari C, Felix A, et al. ESGO/ESTRO/ESP Guidelines for the management of patients with cervical cancer – Update 2023*. International Journal of Gynecological Cancer. 2023 May 1;33(5):649–66.

8. Dheur A, Kakkos A, Danthine D, Delbecque K, Goffin F, Gonne E, et al. Lymph node assessment in cervical cancer: current approaches. Front Oncol. 2024 Nov 11;14:1435532.

9. Mathevet P, Lécuru F, Uzan C, Boutitie F, Magaud L, Guyon F, et al. Sentinel lymph node biopsy and morbidity outcomes in early cervical cancer: Results of a multicentre randomised trial (SENTICOL-2). European Journal of Cancer. 2021 May 1;148:307–15.

10. Van der Zee AGJ, Oonk MH, De Hullu JA, Ansink AC, Vergote I, Verheijen RH, et al. Sentinel node dissection is safe in the treatment of early-stage vulvar cancer. J Clin Oncol. 2008 Feb 20;26(6):884–9.

11. Institut Claudius Regaud. PARa-aOrtic LymphAdenectomy in Locally Advanced Cervical Cancer [Internet]. clinicaltrials.gov; 2025 June [cited 2025 Sept 16]. Report No.: NCT05581121. Available from: https://clinicaltrials.gov/study/NCT05581121

12. Gennigens C, Jerusalem G, Lapaille L, De Cuypere M, Streel S, Kridelka F, et al. Recurrent or primary metastatic cervical cancer: current and future treatments. ESMO Open. 2022 Oct;7(5):100579.

13. Pötter R, Tanderup K, Schmid MP, Jürgenliemk-Schulz I, Haie-Meder C, Fokdal LU, et al. MRI-guided adaptive brachytherapy in locally advanced cervical cancer (EMBRACE-I): a multicentre prospective cohort study. The Lancet Oncology. 2021 Apr;22(4):538–47.

14. Vella G, Hua Y, Bergers G. High endothelial venules in cancer: Regulation, function, and

therapeutic implication. Cancer Cell. 2023 Mar;41(3):527–45.

15. Gennigens C, De Cuypere M, Hermesse J, Kridelka F, Jerusalem G. Optimal treatment in locally advanced cervical cancer. Expert Review of Anticancer Therapy. 2021 June 3;21(6):657–71.

16. Uzan C, Souadka A, Gouy S, Debaere T, Duclos J, Lumbroso J, et al. Analysis of morbidity and clinical implications of laparoscopic para-aortic lymphadenectomy in a continuous series of 98 patients with advanced-stage cervical cancer and negative PET-CT imaging in the para-aortic area. Oncologist. 2011;16(7):1021–7.

17. Acosta Ú, Bebia V, Torné A, Carreras-Dieguez N, Glickman A, Pérez-Benavente A, et al. Topographic mapping of pelvic and aortic lymph node metastases in stage IIIC1r locally advanced cervical cancer: A retrospective study by the Spain-GOG group. Gynecologic Oncology. 2025 July;198:49–54.

18. Hampton HR, Chtanova T. The lymph node neutrophil. Seminars in Immunology. 2016 Apr;28(2):129–36.

19. Streeter PR, Rouse BT, Butcher EC. Immunohistologic and functional characterization of a vascular addressin involved in lymphocyte homing into peripheral lymph nodes. The Journal of cell biology. 1988 Nov 1;107(5):1853–62.

20. Girard JP, Springer TA. High endothelial venules (HEVs): specialized endothelium for lymphocyte migration. Immunology Today. 1995 Sept;16(9):449–57.

21. Vella G, Guelfi S, Bergers G. High Endothelial Venules: A Vascular Perspective on Tertiary Lymphoid Structures in Cancer. Front Immunol. 2021 Aug 17;12:736670.

22. Bekkhus T, Martikainen T, Olofsson A, Franzén Boger M, Vasiliu Bacovia D, Wärnberg F, et al. Remodeling of the Lymph Node High Endothelial Venules Reflects Tumor Invasiveness in Breast Cancer and is Associated with Dysregulation of Perivascular Stromal Cells. Cancers (Basel). 2021 Jan 8;13(2):211.

23. Balsat C, Blacher S, Herfs M, Van De Velde M, Signolle N, Sauthier P, et al. A specific immune and lymphatic profile characterizes the pre-metastatic state of the sentinel lymph node in patients with early cervical cancer. OncoImmunology. 2017 Feb;6(2):e1265718.

24. Peinado H, Zhang H, Matei IR, Costa-Silva B, Hoshino A, Rodrigues G, et al. Pre-metastatic niches: organ-specific homes for metastases. Nat Rev Cancer. 2017 May;17(5):302–17.

25. Gillot L, Lebeau A, Baudin L, Pottier C, Louis T, Durré T, et al. Periostin in lymph node pre-metastatic niches governs lymphatic endothelial cell functions and metastatic colonization. Cell Mol Life Sci. 2022 June;79(6):295.

26. Tewari KS. Cervical Cancer. Longo DL, editor. N Engl J Med. 2025 Jan 2;392(1):56–71.

27. Ogasawara A, Hasegawa K. Recent advances in immunotherapy for cervical cancer. Int J Clin Oncol. 2025 Mar 1;30(3):434–48.

28. Lorusso D, Xiang Y, Hasegawa K, Scambia G, Leiva M, Ramos-Elias P, et al. Pembrolizumab or placebo with chemoradiotherapy followed by pembrolizumab or placebo for newly diagnosed, high-risk, locally advanced cervical cancer (ENGOT-

cx11/GOG-3047/KEYNOTE-A18): overall survival results from a randomised, double-blind, placebo-controlled, phase 3 trial. The Lancet. 2024 Oct;404(10460):1321–32.

29. Ling J, Sun Q, Tian Q, Shi H, Yang H, Ren J. Human papillomavirus 16 E6/E7 contributes to immune escape and progression of cervical cancer by regulating miR-142–5p/PD-L1 axis. Archives of Biochemistry and Biophysics. 2022 Nov 30;731:109449.

30. Martinez A, Voglimacci M, Lusque A, Ducassou A, Gladieff L, Dupuis N, et al. Tumour and pelvic lymph node metabolic activity on FDG-PET/CT to stratify patients for para-aortic surgical staging in locally advanced cervical cancer. Eur J Nucl Med Mol Imaging. 2020 May 1;47(5):1252–60.

31. De Cuypere M, Lovinfosse P, Goffin F, Gennigens C, Rovira R, Duch J, et al. Added value of para-aortic surgical staging compared to 18F-FDG PET/CT on the external beam radiation field for patients with locally advanced cervical cancer: An ONCO-GF study. European Journal of Surgical Oncology. 2020 May;46(5):883–7.

32. Martinez A, Lecuru F, Bizzarri N, Chargari C, Ducassou A, Fagotti A, et al. PARa-aOrtic LymphAdenectomy in locally advanced cervical cancer (PAROLA trial): a GINECO, ENGOT, and GCIG study. International Journal of Gynecological Cancer. 2023 Feb;33(2):293–8.

33. Lin Z, Liu Z, Chen J, Gu H, Liu G, Liu J, et al. Novel anatomical concept and standardized technique for single-port Paraaortic lymphadenectomy in gynecological cancers. Gynecologic Oncology. 2025 Oct 1;201:176–83.

34. deLeeuw RJ, Kost SE, Kakal JA, Nelson BH. The Prognostic Value of FoxP3+ Tumor-Infiltrating Lymphocytes in Cancer: A Critical Review of the Literature. Clin Cancer Res. 2012 May 31;18(11):3022–9.

35. Punt S, van Vliet ME, Spaans VM, de Kroon CD, Fleuren GJ, Gorter A, et al. FoxP3(+) and IL-17(+) cells are correlated with improved prognosis in cervical adenocarcinoma. Cancer Immunol Immunother. 2015 June;64(6):745–53.

36. Li L, Xu XT, Wang LL, Qin SB, Zhou JY. Expression and clinicopathological significance of Foxp3 and VISTA in cervical cancer. Am J Transl Res. 2021 Sept 15;13(9):10428–38.

37. Shang B, Liu Y, Jiang S juan, Liu Y. Prognostic value of tumor-infiltrating FoxP3+ regulatory T cells in cancers: a systematic review and meta-analysis. Sci Rep. 2015 Oct 14;5(1):15179.

Table 1. **Risk factors for disease relapse identified by univariate and multivariate analyses.** SCC: squamous cell carcinoma; HR: hazard ratio with [95% CI]; PH: proportional hazards. Variables that showed association with relapse risk at a p-value of <0.1 in univariable analysis were included in the multivariable model (variables included are in red).

Figure 1. **Study design and clinico-pathological features of patients with locally advanced cervical cancer (LACC). A, B**. Schematic representation of the para-aortic (A) and pelvic (B) regions in patient with cervical cancer. The retrospective cohort includes primary tumor and para-aortic (PAoLN) samples from patients with LACC (N=155), stratified by the absence (PAoLN-) or presence (PAoLN+) of metastatic PAoLNs assessed through histological examination. Pelvic disease status was defined by positron emission tomography (PET) as negative (pPET-) or positive (pPET+) (B). **C.** Workflow of immunohistochemical analyses of patient biopsies. Whole tissue sections were imaged and computationally analyzed using QuPath software. Univariate and multivariate statistical analyses were performed to identify predictive signatures integrating biological parameters with clinical data. **D.** The cohort included 155 patients: 18 patients had metastatic PAoLN and 137 did not (regardless of pelvic PET scan status). Univariate and multivariate analyses were performed in the subgroup of 130 patients who received uniform treatment with concomitant chemoradiotherapy (CCRT) followed by image-guided brachytherapy (IGBT). **E**. Kaplan-Meier plots showing the impact of pPET status on progression-free survival (PFS) in patients treated with CCRT and IGBT. Log-rank test *p<0.05.

Figure 2. **Immunohistochemical analyses of primary tumors. A**. Computerized segmentation of the tumor regions. The tumor compartment corresponds to cytokeratin positive cells (cyan). The stroma is cytokeratin negative part containing αSMA positive structures (green). **B-C**. Illustrations of CD4 (yellow) and CD8 (red) T cells (B), and CD66b+ (yellow) and FOXP3+ (magenta) cells (C). **D-H.** Histograms present the quantifications of immune cell infiltration expressed as cell density in pPET- (N=46) and pPET + (N=45) patient subgroups: CD4/CD8 ratio (**D**), CD4 density (**E**), CD8 density (**F**), FOXP3+ cells (**G**), CD66b+ cells (**H**). Data are represented by median with interquartile ranges. Mann-Whitney U tests, *p<0.05; **p<0.01; ***p<0.001; ****p<0.0001. **I-P:** Relationship between tumor-associated HEVs (TA-HEVs) and T cell infiltration in primary tumors. **I.** Representative image showing PNAd+ αSMA+ vessels (TA-HEVs) within the tumor stroma, as identified in panel A. **J.** Tumor samples from 91 patients were separated into four classes based on PNAd+ αSMA+ vessel density in tumor stroma: I (0/mm²), II (0-1.173/mm²), III (1.173-4.362/mm²) and IV (4.362-22.644/mm²). **K.** Density of TA-HEVs in pPET- and pPET+ patients. **L.** Distribution (%) of TA-HEV classes in pPET- and pPET+ subgroups. **M-P**. Spearman correlations between TA-HEVs and immune cell infiltration represented by either TA-HEV classes (histograms, top) or TA-HEV number (scatter plots, bottom): CD8+ cells (**M**), CD4+ cells (**N**), CD66b+ cells (**O**) and FOXP3+ cells (**P**). Correlation coefficients (r_s) and p-values are indicated. Data are shown as median with interquartile ranges. Mann-Whitney U or Kruskal-Wallis tests, *p<0.05.

Figure 3. **Impact of pelvic PET scan status on PAoLN remodeling**. **A-I:** Densities of immune and vascular parameters assessed by IHC (as described in Figure 3) were compared between pPET- (N=67) and pPET+ (N=62) patient subgroups: germinal centers (number/mm²) (**A**), CD4/CD8 ratio (**B**), CD4+ cell density (**C**), CD8+ cell density (**D**), FOXP3+ cells/mm² (**E**), FOXP3+Ki67+ cells/mm² (**F**), CD66b+ cells/mm² (**G**), NET density (**H**), percentage of dilated HEVs (**I**). Dilated HEVs were defined as PNAd+ vessels with a lumen > 20μm,

measured as the smallest diameter (as illustrated in the right). **J-M**: Spearman correlations between HEV dilatation and CD4+ (**J**), CD8+ (**K**), CD66b+ (**L**) and FOXP3+ (**M**) cell density. Correlation coefficients (r_s) and p-values are indicated. Data are represented as medians with interquartile ranges. Mann-Whitney U tests, *p<0.05; **p<0.01.

Figure 4. **Multivariate prognostic model integrating PET status and PAoLN features.** **A**. Time-dependent area under the curve (AUC) for PFS, with 95% confidence intervals (CI) indicated by dashed lines. **B**. Nomogram for PFS prediction. Each covariate is assigned a weighted score proportional to its relative contribution to the model. The total score corresponds to an individualized estimated probability to remain progression-free at 12, 24, and 36 months. **C**. Cumulative incidence functions for the overall cohort (N=123) and stratified by pPET+ and pPET- subgroups.

Figure 5. **Predictive combination of factors in pPET+ and pPET- patients. A, D**. Schematic illustration of the strongest predictive associations of clinical and biological variables. The percentage and number of patients experiencing relapse are indicated. **B, E**. Kaplan-Meier curves depicting progression-free survival according to the main predictive combination in pPET+ (**B**) and pPET- (**E**) patients. **C, F**. Diagnostic performance of the main predictive combination in pPET+ (**C**) and pPET- (**F**) patients with sensitivity, specificity, positive predictive value (PPV), negative predictive value (NPV), and overall accuracy.

Locally Advanced Cervical Cancer

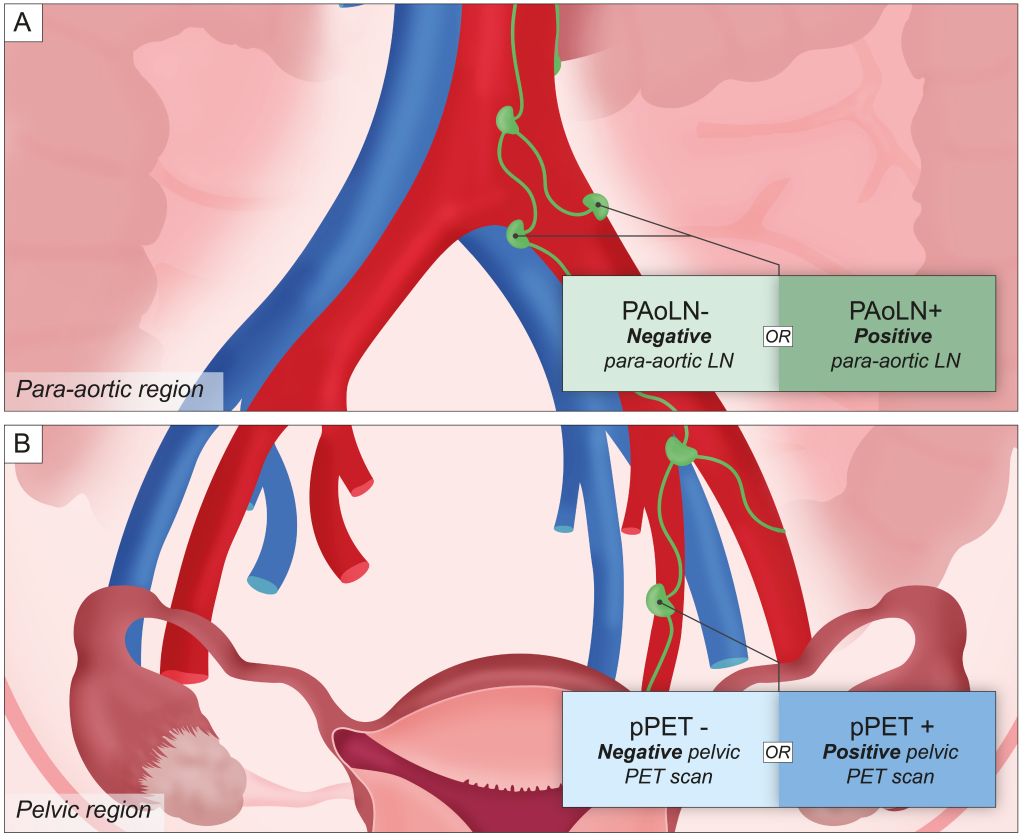

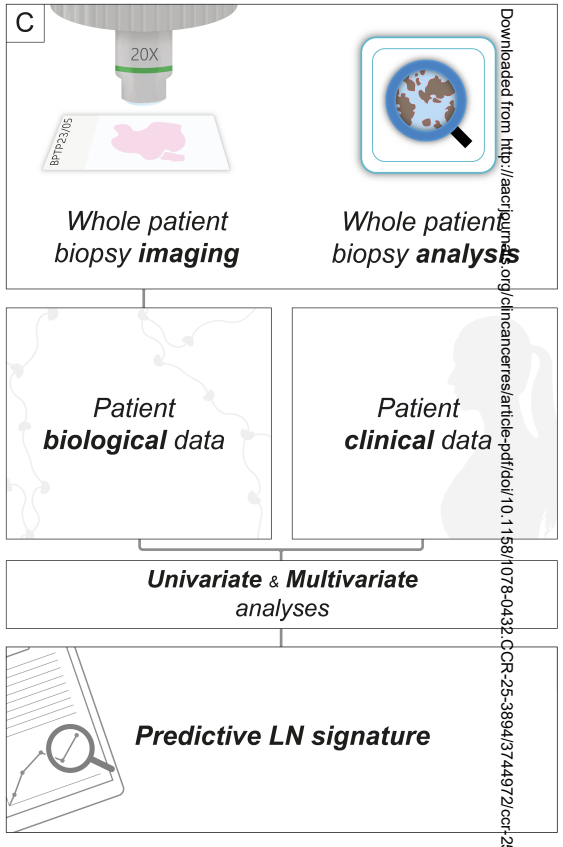

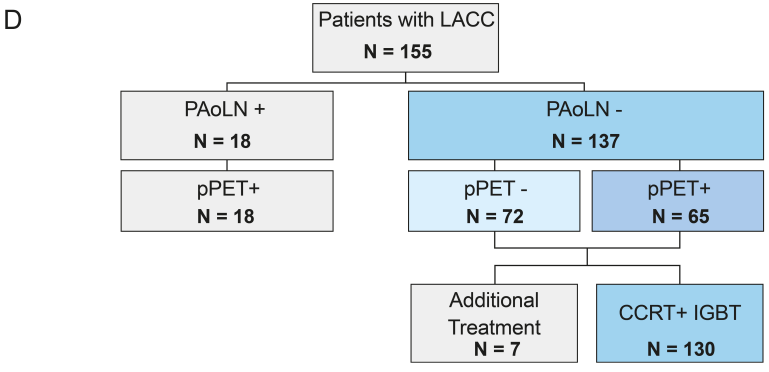

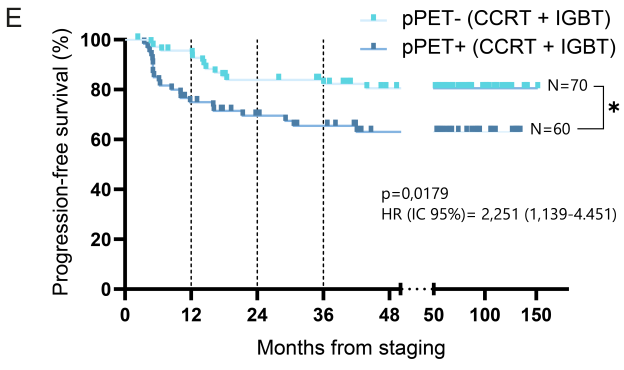

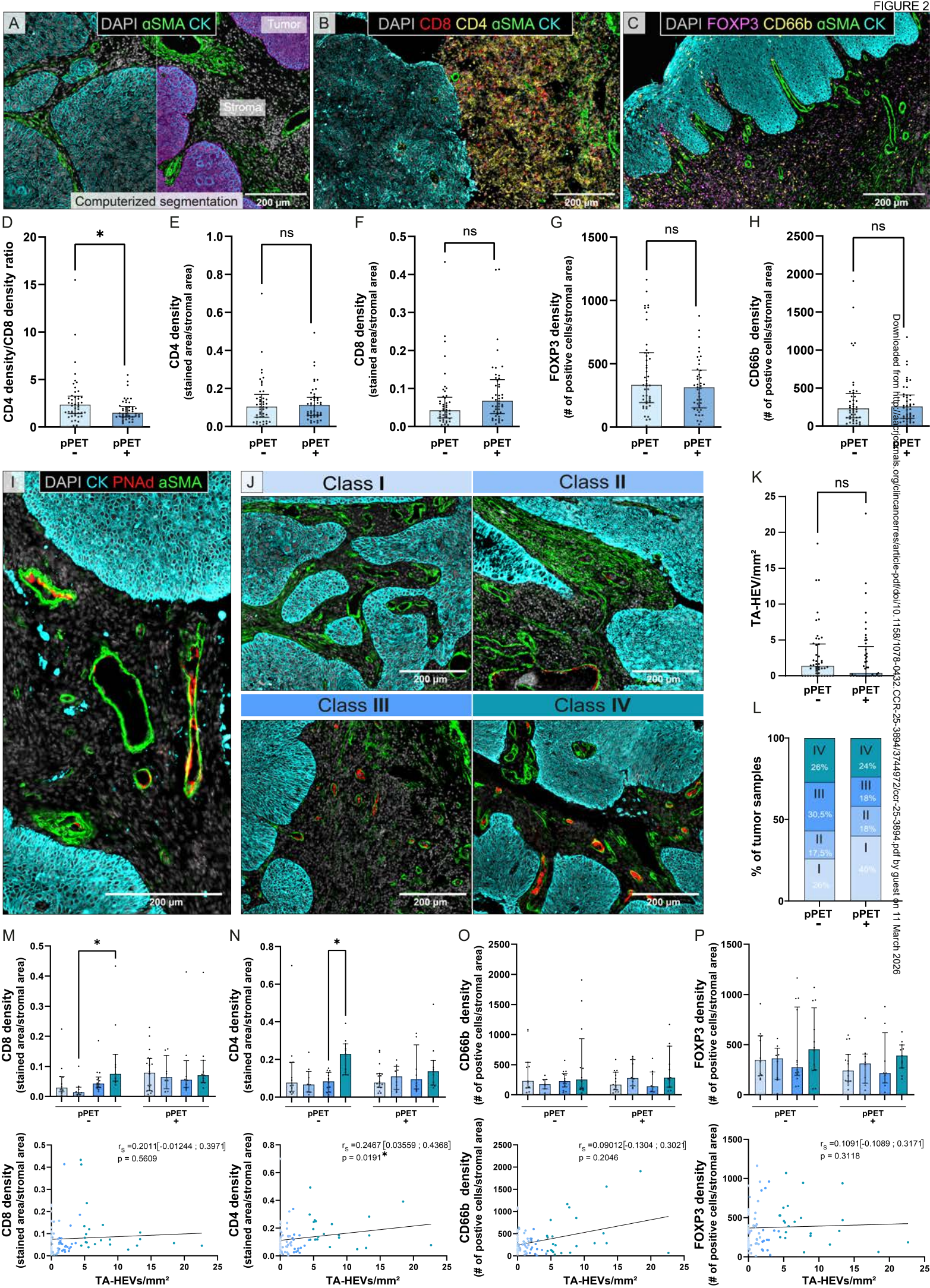

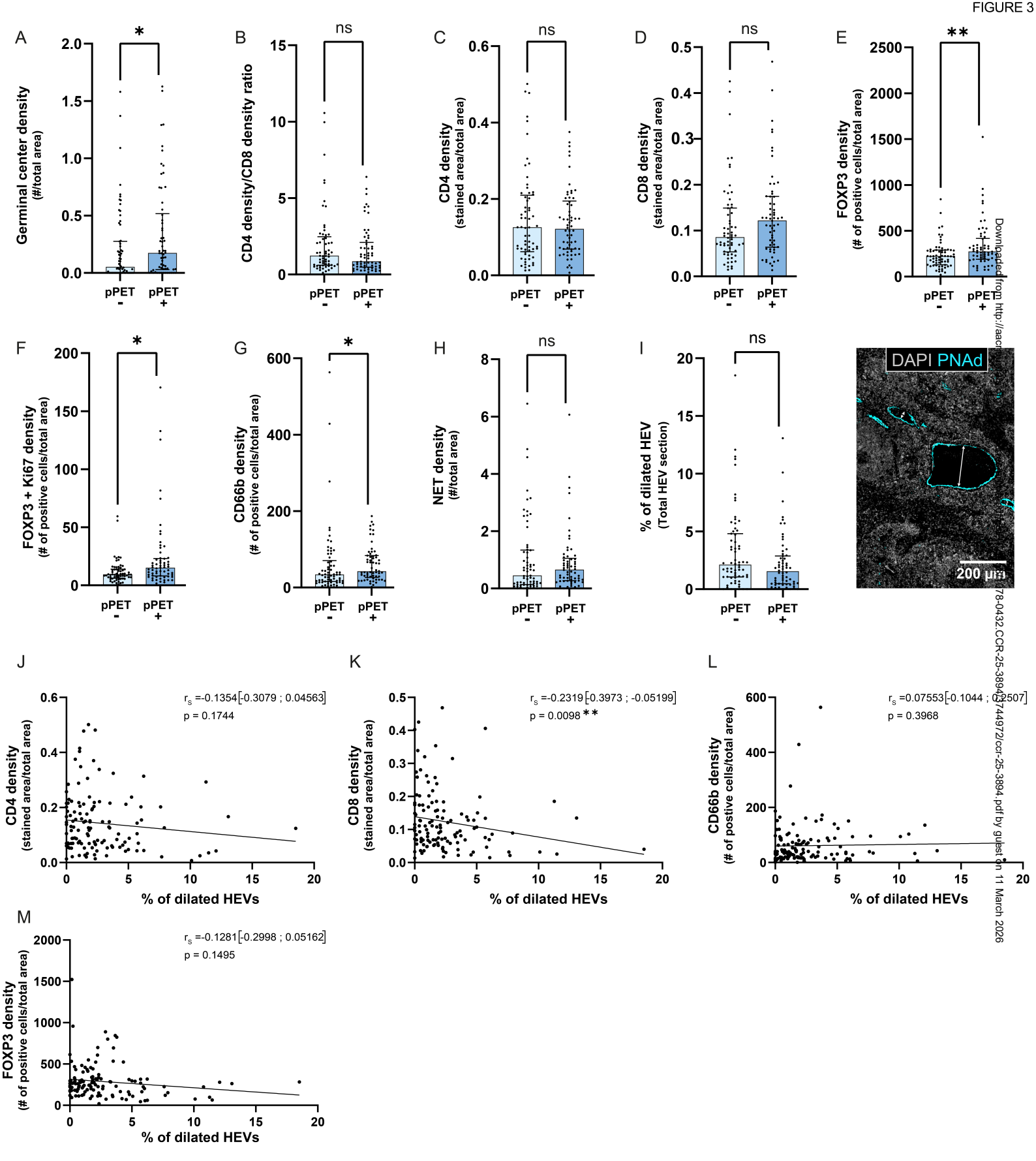

A

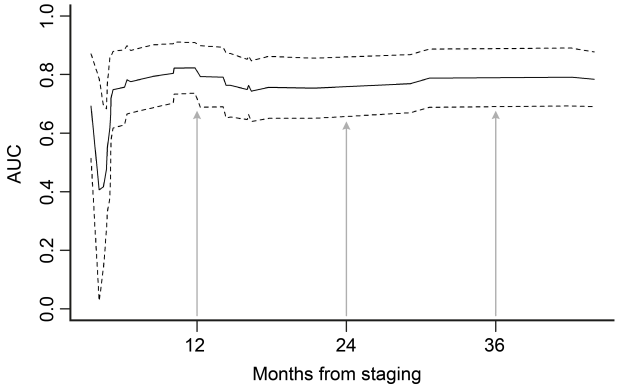

Months	AUC [95%CI]
12	0.8231 [0.7369-0.9094]
24	0.7525 [0.6499-0.8551]
36	0.7848 [0.6851-0.8846]

B

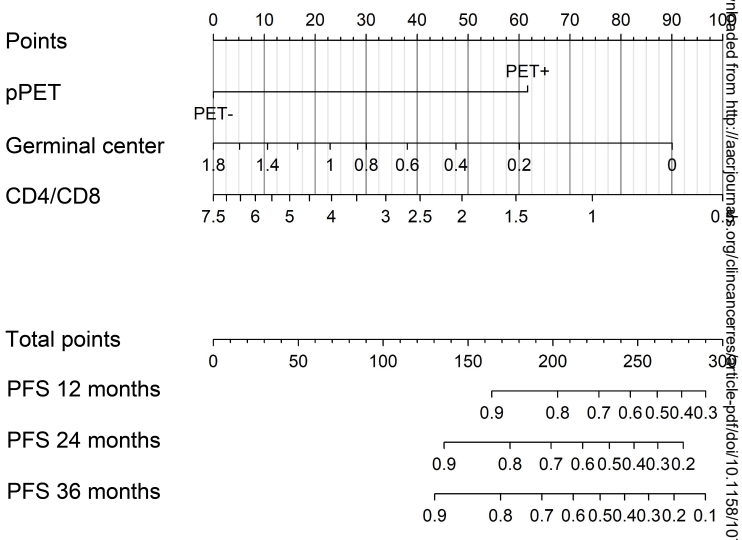

C

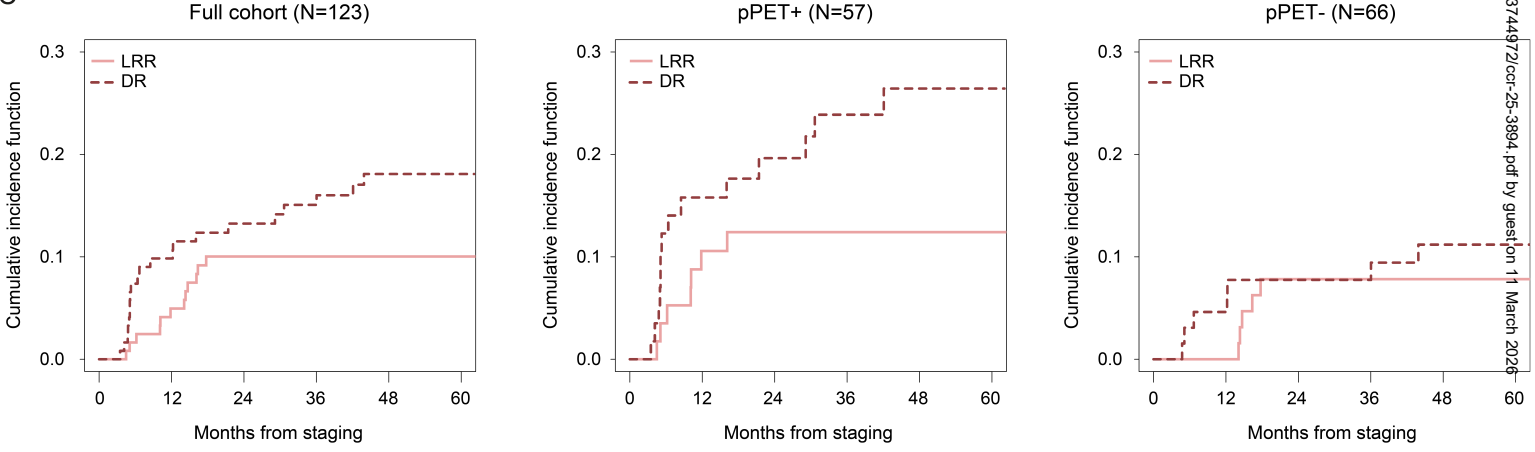

pPET+

A

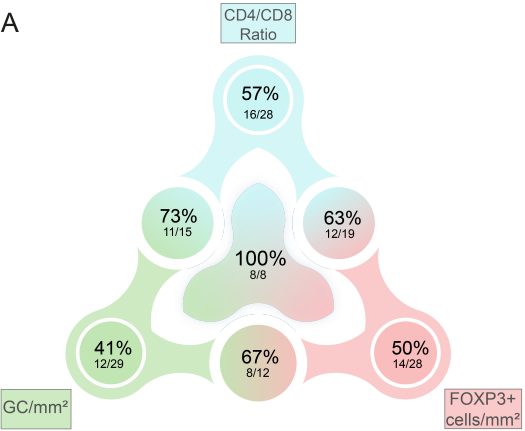

B

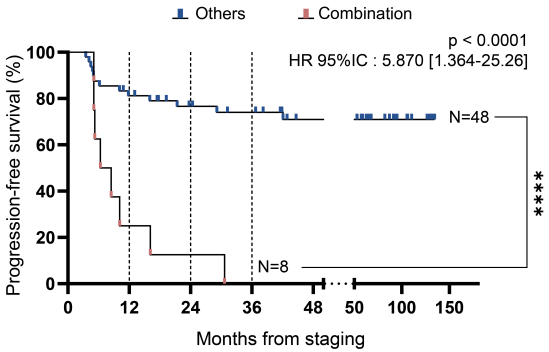

C

NPV [95%CI]	PPV [95%CI]
0.73 [0.58-0.85]	1.00 [0.63-1.00]
Specificity [95%CI]	**Sensitivity [95%CI]**
1.00 [0.90-1.00]	0.38 [0.18-0.62]
Accuracy [95%CI]	
0.77 [0.64-0.87]	

pPET-

D

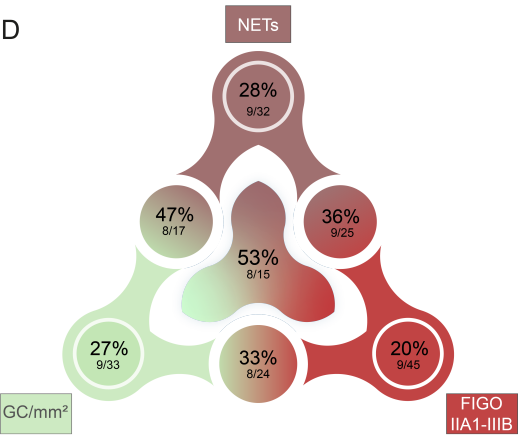

E

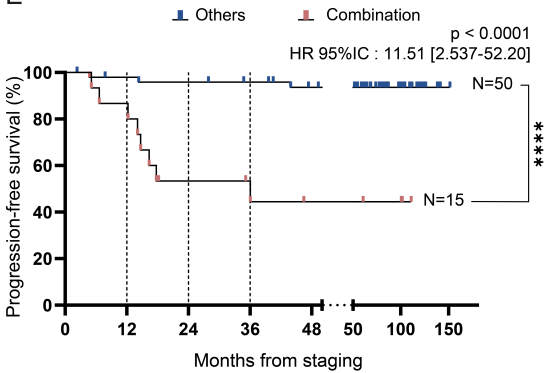

F

NPV [95%CI]	PPV [95%CI]
0.94 [0.83-0.99]	0.53 [0.27-0.79]
Specificity [95%CI]	**Sensitivity [95%CI]**
0.87 [0.75-0.95]	0.73 [0.39-0.94]
Accuracy [95%CI]	
0.85 [0.74-0.92]	

Table 1

PAoLN- pPET- (N=66)

Variable	p-value	HR [95%CI]	PH test
Non-SCC vs SCC	0.68	1.313 [0.355-4.850]	0.6398
FIGO IIA1-IIIB vs IB3	0.54	1.608 [0.352-7.342]	0.6888
Age	0.26	0.973 [0.927-1.021]	0.4048
Tumor size	0.46	1.018 [0.972-1.065]	0.3215
Neutrophils/mm²	0.29	1.313 [0.793-2.173]	0.1777
NETs/mm²	0.015	2.768 [1.215-6.304]	0.9733
FOXP3+/mm²	0.78	1.138 [0.459-2.821]	0.1303
FOXP3+KI67+/mm²	0.76	1.119 [0.548-2.286]	0.2341
Germinal center/mm²	0.089	0.102 [0.007-1.413]	0.2095
CD4/CD8 ratio	0.047	0.497 [0.250-0.989]	0.7125
/			
/			
Dilated HEV	0.88	1.048 [0.560-1.959]	0.1466

PAoLN- pPET+ (N=57)

Variable	p-value	HR [95%CI]	PH test
Non-SCC vs SCC	0.09	2.336 [0.853-6.395]	0.9979
/			
Age	0.53	0.986 [0.943-1.031]	0.8669
Tumor size	0.53	1.010 [0.978-1.044]	0.1981
Neutrophils/mm²	0.43	1.222 [0.742-2.011]	0.0949
NETs/mm²	0.90	1.064 [0.401-2.825]	0.4163
FOXP3+/mm²	0.040	1.918 [1.029-3.575]	0.1512
FOXP3+KI67+/mm²	0.018	1.668 [1.093-2.544]	0.0586
Germinal center/mm²	0.17	0.395 [0.106-1.472]	0.4830
CD4/CD8 ratio	0.0097	0.506 [0.302-0.848]	0.0455
CD4/CD8 ratio (corrected)	0.49	0.759 [0.347-1.656]	
CD4/CD8 ratio x time	0.20	0.967 [0.917-1.019]	
Dilated HEV	0.60	0.855 [0.474-1.543]	0.2146

PAoLN- (N=123)

	Univariate			Multivariate			Bootstrap (500 resamples)
Variable	**p-value**	**HR [95%CI]**	**PH test**	**p-value**	**HR [95%CI]**	**C-index**	**C-index [95%CI]**
pPET	0.013	2.452 [1.204-4.990]	0.16	0.0033	3.299 [1.488-7.315]	0.7434	0.7536 [0.666-0.841]
Non-SCC vs SCC	0.2395	1.613 [0.727-3.576]	0.93	-			
FIGO IIA1-IIIB vs IB3	0.044	1.632 [0.358-7.448]	0.96	-			
FIGO IIIC1-IVA vs IB3		3.620 [0.848 ˙15.449]	0.53	-			
FIGO IIA1-IIIB vs IIIC1-IVA		0.451 [0.212-0.959]	0.19	-			
Age	0.22	0.980 [0.950-1.012]	0.53	-			
Tumor size	0.058	3.452 [0.961-12.399]	0.028	-			
Tumor size (corrected)	0.0088	17.02 [2.043-141.77]					
Tumor size x time	0.0572	1.003 [0.797-1.003]					
Neutrophils/mm²	0.096	1.327 [0.951-1.851]	0.52	-			
NETs/mm²	0.071	1.712 [0.955-3.071]	0.15	-			
FOXP3+/mm²	0.015	1.900 [1.132-3.191]	0.70	-			
FOXP3+KI67+/mm²	0.0032	1.729 [1.202-2.489]	0.81	-			
Germinal center/mm²	0.097	0.379 [0.120-1.193]	0.57	0.0355	0.273 [0.081-0.915]		
CD4/CD8 ratio	0.0004	0.483 [0.323-0.720]	0.16	0.0010	0.490 [0.320-0.748]		
Dilated HEV	0.47	0.857 [0.565-1.301]	0.58	-			